

Uniform Rectangular Antenna Array Design and Calibration Issues for 2-D ESPRIT Application

Gerd Sommerkorn^(1,2), Dirk Hampicke⁽¹⁾, Ralf Klukas⁽³⁾, Andreas Richter⁽¹⁾,
Axel Schneider⁽¹⁾, Reiner Thomä⁽¹⁾

⁽¹⁾ FG EMT, Ilmenau Technical University
P.O.Box 100565, D-98684 Ilmenau, Germany
Phone: +49 3677 69 1157 Fax: +49 3677 69 1113
eMail: som@e-technik.tu-ilmenau.de
WWW: <http://www-emt.tu-ilmenau.de>

⁽²⁾ MEDAV Digitale Signalverarbeitung GmbH
Gräfenberger Straße 34, D-91080 Uttenreuth, Germany
WWW <http://www.medav.de>

⁽³⁾ Dresden University of Technology
eMail: klukas@ifn.et.tu-dresden.de

Abstract

In this paper the use of uniform rectangular antenna arrays for spatial signal processing in mobile radio is investigated. The regular structure of such an antenna array together with the uniform responses of all of its elements allows the application of the 2-D unitary ESPRIT algorithm for superresolution direction of arrival estimation. However, since real antenna arrays suffer from different impairments that distort the ideal antenna response, the expected superresolution gain can only be reached if sophisticated antenna array design and calibration methods are applied. To study these effects we have built up a patch antenna array with 8 by 8 elements and minimum element coupling and employed it for wideband vector radio channel sounding at 5.2 GHz. The design method for this array is described. Furthermore, a 2-D calibration approach based on a precision measurement procedure in an anechoic environment and a nullspace based parameter estimation algorithm is given in order to mitigate the remaining coupling. Measurement results are reported to demonstrate the performance. Possible applications include the determination of azimuth and elevation angle of arrival for wideband vector radio channel sounding.

1 Introduction

Smart antenna principles are considered to improve the system performance of mobile radio links substantially. A large variety of spatial signal processing methods is currently being investigated, including beam-forming, direction-of-arrival (DoA) estimation, adaptive space-time equalization, or interference cancellation. Generally, the design of the smart antenna has a major influence on the resulting performance. Uniform linear arrays (ULA) are used to resolve the azimuthal angle of the impinging waves while uniform rectangular arrays (URA) additionally allow to resolve the elevation. Due to the regular rectangular structure of a URA 2-D ESPRIT algorithms [4] are well suited for parameter estimation. Moreover, 2-D spatial smoothing can be carried out easily in order to cope with coherent waves (which is especially important in complicated micro- or picocell environments).

Since real antenna arrays suffer from lots of impairments (e.g. mechanical and electrical manufacturing tolerances, amplitude and phase mismatch in antenna feeding, coupling between antenna elements, finite size effects etc.), which will result in nonuniform beam patterns and lead to serious performance degradation of the parameter estimation algorithm, an antenna calibration procedure is necessary. Particularly the ESPRIT algorithm expects identical array responses, since it is based on the shift-invariance property of two subarrays. Moreover, spatial subarray smoothing, which in case of coherent waves is required for subspace-based DoA estimation, can only be applied if the antenna element responses are uniform. This imposes a restriction to the ESPRIT and the MUSIC algorithm. Measurements with multiple sources in a well defined environment have shown that also the resolution of closely spaced coherent sources is reduced dramatically [2]. If the MUSIC algorithm is applied for noncoherent sources, only the precise knowledge of the array beam patterns is sufficient and

no further sophisticated calibration is necessary. In [1], [3] a calibration procedure for ULAs has been described which is based on a (direction independent) error model depicted in Fig. 1. The coefficients crossing the elements cause a output correlation whereas the straight coefficients stand for a weighted output.

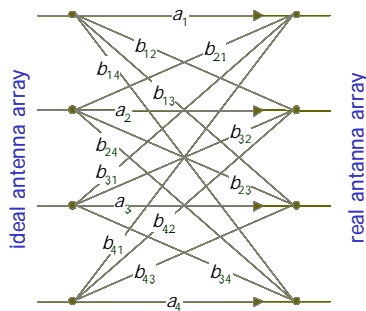


Fig. 1 Scheme of the error model

From reference measurements in a well defined anechoic environment and a subsequent parameter estimation step, a calibration matrix was constructed which is multiplied to the distorted array output. The result is a more smooth, uniform array response which can be handled as an ideal uniform array output by the subsequent DoA estimation algorithm (i.e. the calibration effectively decouples the antennas).

In this paper we will investigate design and calibration issues for URAs employing the 2-D ESPRIT algorithm. For this purpose a real patch antenna array with 8 by 8 elements and minimum element coupling was constructed to be used for wideband vector radio channel sounding at 5.2 GHz [2]. At first in section 2 the design of the patch antenna array is described with focus on the minimization of the inter-element coupling. Influence of remaining coupling is further reduced by a 2-D calibration approach. The underlying calibration algorithm which is an extension of the 1-D algorithm described in [3] and a suitable measurement procedure are given in section 3. Finally, measurement examples are presented which show the resulting beam patterns and the DoA estimation error for a single source and for two coherent sources. The multidimensional ESPRIT algorithm is employed for the parameter estimation because of its computational efficiency.

2 Uniform Rectangular Antenna Array Design

In the following the design of an 8 by 8 element uniform rectangular array will be described. This prototype array is composed of removable antennas that are separately mounted on a common ground plane. The array elements are designed for 5.2 GHz with a bandwidth of 120 MHz and a half-power

beamwidth of 60° in elevation and 120° in azimuth. The prescribed high isolation between adjacent elements requires a careful investigation of the near-field properties of the antennas and the corresponding coupling mechanisms.

Since the ESPRIT algorithm supposes point sources in both aperture dimensions of the URA, patch antennas have been selected. They offer a relatively concentrated and uniform phase center in the horizontal and the vertical direction. The patch structure should be as small as possible, and if necessary, the substrate permittivity has to be increased. In addition, special care has to be taken to ensure half a wavelength separation between the elements. The substrate has to be chosen carefully regarding its permittivity and thickness because there is a trade-off between a small radiating surface and a high element-to-element isolation. The feeding is accomplished by a coaxial line perpendicular from the back-side of the patch substrate which, compared to other feeding systems, helps to decrease element cross-coupling.

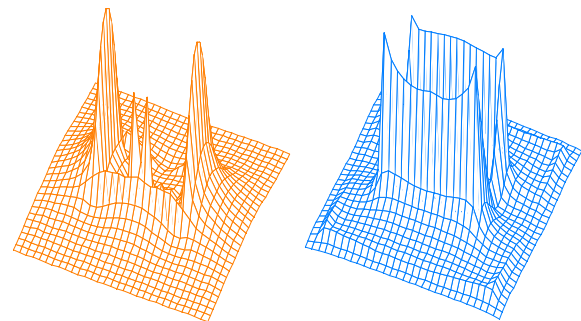


Fig. 2 Magnitudes of the distribution of H- (left) and E-field (right) for a single patch element on a substrate plate

Fig. 2 shows the magnitudes of E- and H-fields on a small substrate plate with a radiating metal pad. It can be seen that the H-field has a low magnitude at the horizontal edges of the substrate whereas the E-field obviously is increased. Hence the coupling mechanism between an element and its neighbors depends on the arrangement and the distance relative to each other. Furthermore, radiation coupling as well as coupling via surface wave modes are strongly related since propagation of surface waves is also strongly dependent on the chosen substrate permittivity. If a common contiguous substrate plate were used for all radiators a trade-off has to be found between radiation coupling due to leaky waves and directly propagating surface waves. Even if the antenna elements were mounted on individual substrates, any discontinuity, for example a substrate edge, would transform surface waves into leaky waves which will deteriorate the radiation pattern.

Fig. 3 shows the calculated magnitudes of H- and E- near field for a two-patch column at the surface of the array. One patch element is excited and the other one is terminated by its characteristic impedance of 50Ω . The local field maxima at the edges of the terminated elements caused by coupling effects can be observed clearly.

As an experimental prototype the array was built up of separate elements in order to gain flexibility. The backside metallization of the substrate of the elements acts as a ground plane. A large metal plate is used as a mounting plane, which gives mechanical support for the whole assembly. But it has also an influence on the radiation pattern shaping. Therefore, an absorber mask has been placed between both planes attenuating the backward radiation of the patches and thus minimizing any interference between forward directed and reflected radiation. It also reduces the magnitude of the fringing fields at the substrate edges.

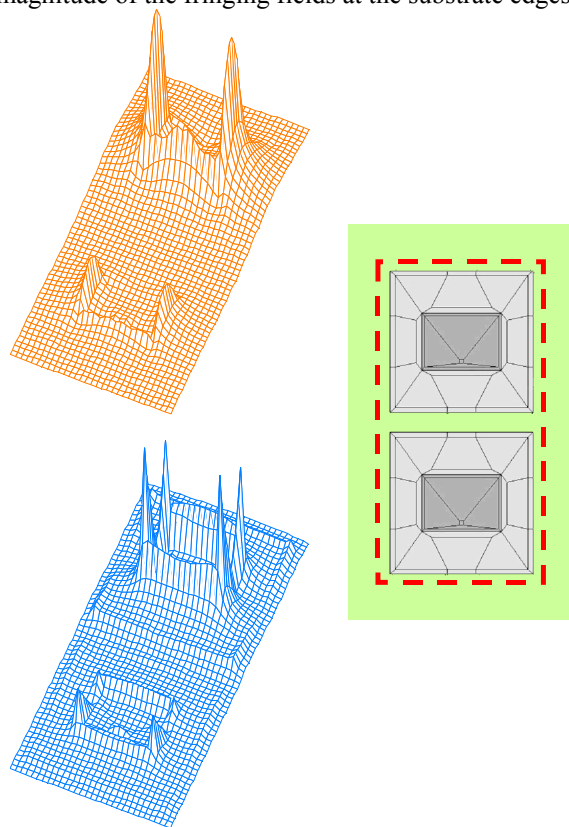


Fig. 3 Magnitudes of H- (top left) and E-field distribution (bottom left) for a two-patch arrangement, scheme (right)

A simulation model of the array and a comparison between predicted and measured horizontal diagrams of one element are depicted in Fig. 4.

In order to minimize the fringing field because of the finite array size, the realized URA actually consists of 14 by 14 antennas. The outer 3 rows/columns of them represent dummy elements, which are internally

terminated with 50Ω . Fig. 5 shows the complete array.

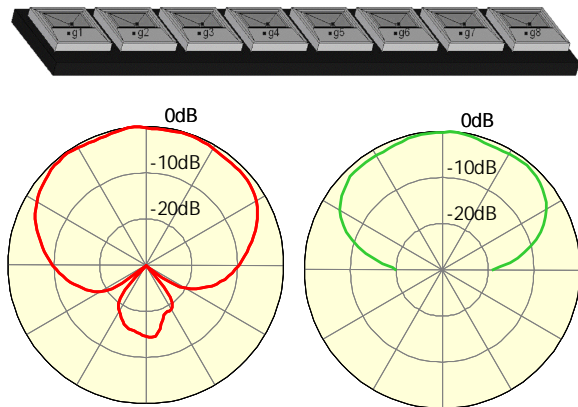


Fig. 4 Horizontal diagram for an element in the middle of the patch row; calculated (left) and measured (right)

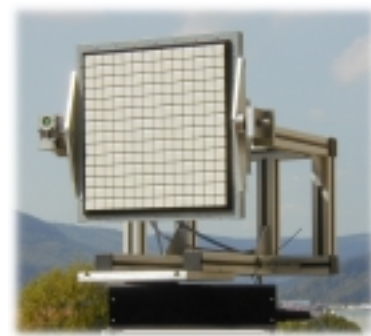


Fig. 5 8 by 8 (resp. 14 by 14) element uniform rectangular antenna array @ 5,2 GHz

3 Uniform Rectangular Antenna Array Calibration

The basic idea of the applied calibration algorithm has been described in [1] and was adopted for channel sounder application in [3] and [5].

3.1 Coordinate System Definition

Before the calibration algorithm and procedure are presented some remarks on the geometrical basics should be derived. There are some major differences between ULAs and URAs regarding the relations between the directions of arrival and the angles of intersection resulting from the plane wavefront projection onto the array aperture.

Considering a URA located within the y - z -plane (columns parallel to the z -axis; rows parallel to the y -axis), the phase characterization along the columns is denoted by θ and the phase characterization along the rows is denoted by φ (corresponding to the angles of intersection). Both, θ and φ depend on the direction

of the source that is described by the elevation α and azimuth β (cf. Fig. 6).

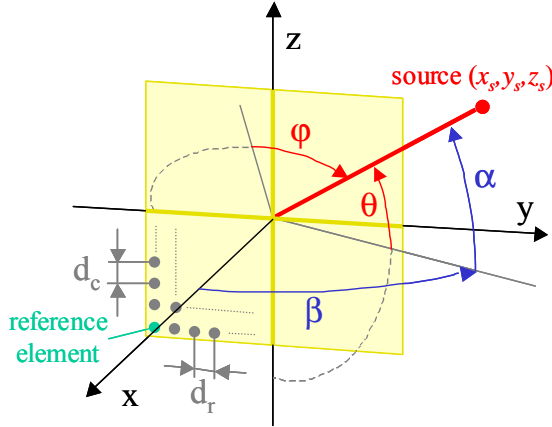


Fig. 6 Scheme of a URA

It can be seen clearly that α is equal to θ and therefore the following expression can be stated

$$\sin \theta = \sin \alpha, \quad (1)$$

whereas β is a function of θ and φ . Beginning with

$$\sin \varphi = \frac{y_s}{\sqrt{x_s^2 + y_s^2 + z_s^2}} \quad \text{and} \quad \sin \alpha = \frac{z_s}{\sqrt{x_s^2 + y_s^2 + z_s^2}}$$

the following expression can be given:

$$\sin \varphi = \frac{y_s}{z_s} \sin \alpha. \quad (2)$$

$$\text{Using } \cos \beta = \frac{x_s}{\sqrt{x_s^2 + y_s^2}} \quad \text{and} \quad \tan \alpha = \frac{z_s}{\sqrt{x_s^2 + y_s^2}}$$

combined to $\tan \alpha = \frac{z_s}{x_s} \cos \beta$, (2) can be rewritten to:

$$\sin \varphi = \frac{y_s \sin \alpha \cos \beta}{x_s \tan \alpha} = \frac{y_s}{x_s} \cos \alpha \cos \beta. \quad (3)$$

With $\tan \beta = \frac{y_s}{x_s}$, (3) yields:

$$\sin \varphi = \sin \beta \cos \alpha. \quad (4)$$

Hence the phase characterization φ of a fixed URA depends on both, the elevation and the azimuth angle of the source.

However, it can be necessary to tilt the URA in its columns (rotation about the y-axis) and its rows (rotation about the z-axis) while the source should be on a fixed location. With it there is the demand to find another description of (1) and (4) in dependence on the URA orientation.

Fig. 7 depicts the modified version of Fig. 6. The elevation α and azimuth β of the source have been set to zero while the URA orientation, characterized by

the normal vector, becomes out of zero for both, the tilt angle η and the rotation angle ρ .

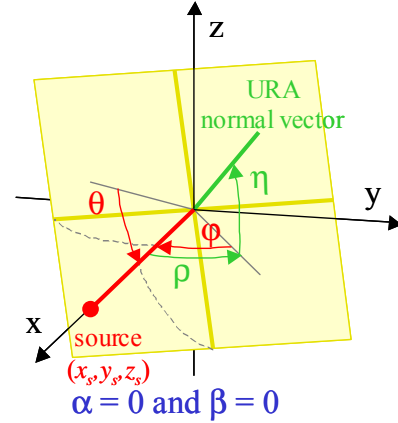


Fig. 7 Scheme of a rotated URA

Regarding the source this modification corresponds to a simple coordinate transformation which can be done using the following two rotation matrices:

$$\mathbf{Rot}_y = \begin{bmatrix} \cos \eta & 0 & -\sin \eta \\ 0 & 1 & 0 \\ \sin \eta & 0 & \cos \eta \end{bmatrix} \quad \text{and}$$

$$\mathbf{Rot}_z = \begin{bmatrix} \cos \rho & -\sin \rho & 0 \\ \sin \rho & \cos \rho & 0 \\ 0 & 0 & 1 \end{bmatrix}.$$

After applying the rotation matrices the new source direction can be described by α' and β' with:

$$\sin \alpha' = -\cos \beta \cos \alpha \cos \rho \sin \eta - \sin \beta \cos \alpha \sin \rho \sin \eta + \sin \alpha \cos \eta \quad (5)$$

and

$$\tan \beta' = (-\cos \beta \cos \alpha \sin \rho + \sin \beta \cos \alpha \cos \rho) \cdot (\cos \beta \cos \alpha \cos \rho \cos \eta + \sin \beta \cos \alpha \sin \rho \sin \eta + \sin \alpha \sin \eta)^{-1}. \quad (6)$$

For $\alpha = \alpha_0 = 0$ and $\beta = \beta_0 = 0$ (5) equations (6) simplify to:

$$\sin \alpha'_{\alpha_0, \beta_0} = -\sin \eta \cos \rho \quad (7)$$

$$\tan \beta'_{\alpha_0, \beta_0} = -\frac{\tan \rho}{\cos \eta}. \quad (8)$$

Utilizing (7) in (1) the phase characterization θ yields:

$$\sin \theta = \sin \alpha'_{\alpha_0, \beta_0} \quad (9)$$

$$\sin \theta = -\sin \eta \cos \rho$$

Analogous, the phase characterization φ results with (8) and (4) in:

$$\begin{aligned}\sin \varphi &= \sin \beta'_{\alpha_0, \beta_0} \cos \alpha'_{\alpha_0, \beta_0} \\ \sin \varphi &= \tan \beta'_{\alpha_0, \beta_0} \sin \alpha'_{\alpha_0, \beta_0} \cos \beta'_{\alpha_0, \beta_0} \frac{\cos \alpha'_{\alpha_0, \beta_0}}{\sin \alpha'_{\alpha_0, \beta_0}} \\ \sin \varphi &= -\sin \rho\end{aligned}\quad (10)$$

It can be seen that the description of θ and φ in dependence on the URA orientation has been exchanged (except the sign) compared with that of the source direction.

3.2 Calibration Algorithm

For a single planar wavefront with the complex-valued pathweight γ the column array steering vector

$$\mathbf{a}_c(\theta) = [1 \quad e^{-j2\pi\frac{d_c}{\lambda}\sin\theta} \quad \dots \quad e^{-j2\pi(M-1)\frac{d_c}{\lambda}\sin\theta}]^T \quad (11)$$

and the row array steering vector

$$\mathbf{a}_r(\varphi) = [1 \quad e^{-j2\pi\frac{d_r}{\lambda}\sin\varphi} \quad \dots \quad e^{-j2\pi(N-1)\frac{d_r}{\lambda}\sin\varphi}]^T \quad (12)$$

of the URA result. The array is characterized by M rows and N columns. The spacing within a row is denoted by d_r and that of a column by d_c . λ corresponds to the wavelength of the carrier frequency. The product of both steering vectors leads to the array steering matrix $\mathbf{A}(\theta, \varphi) = \mathbf{a}_c(\theta)\mathbf{a}_r(\varphi)^T$. Using the vector valued operator $\text{vec}\{\bullet\}$, which maps a m -by- n -matrix to a $m \cdot n$ -dimensional column vector by stacking the columns of the matrix, the array steering matrix may be transformed to a 2-D array steering vector $\mathbf{a}(\theta, \varphi) = \text{vec}\{\mathbf{A}(\theta, \varphi)\}$.

The array response results in $\mathbf{x} = \mathbf{a}(\theta, \varphi)\gamma$. In a more realistic way the measured URA output is modelled by

$$\tilde{\mathbf{x}} = \mathbf{K}\mathbf{a}(\theta, \varphi)\gamma + \mathbf{n} \quad (13)$$

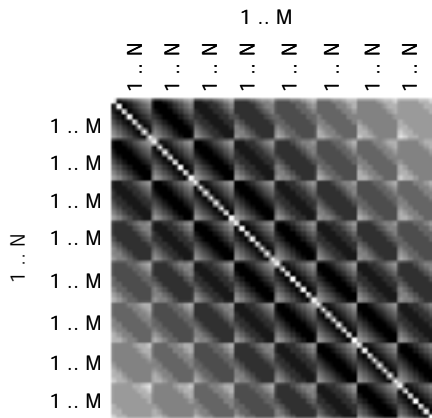


Fig. 8 Error matrix structure in principle ($M=8$; $N=8$)

The array imperfections are described by an $(M \times N) \times (M \times N)$ error matrix \mathbf{K} . This error matrix in its main diagonal directly describes amplitude and phase mismatches at the antenna outputs. The secondary

diagonals represent the mutual output correlation introduced, e.g. by electro-magnetic coupling mechanisms between the antenna elements. In fact, the error matrix performs a mapping of the error-free array output onto the disturbed array output. As a result the matrix \mathbf{K} becomes a nested two-dimensional matrix structure like depicted in Fig. 8. The gray level in the figure relative indicates the nominal coupling magnitude (black corresponds to strong coupling) which depends on the distances between the elements. The aim of the calibration algorithm is to estimate a calibration matrix $\mathbf{K}_{cal} = \mathbf{K}^{-1}$ that effectively compensates the imperfections if applied to the URA output. The proposed algorithm to estimate \mathbf{K}_{cal} is based on the idea, that for an error-free URA a set of orthogonal 2-D null steering matrices $\mathbf{c}_\mu(\theta, \varphi)$ with $\mu=1(1)MN-1$ does exist. They span the equivalent nullspace of the reference source response vector $\mathbf{a}(\theta, \varphi)$. In the measured case that nulling property $0 = \mathbf{c}_\mu^H \mathbf{x} \mathbf{c}_\mu$ will no longer hold. With the calibration matrix \mathbf{K}_{cal} applied to $\tilde{\mathbf{x}}$, the remaining mean squared error (MSE)

$$\varepsilon^2(\mathbf{K}_{cal}) = \sum_{\mu=1}^{MN-1} \mathbf{c}_\mu^H \mathbf{K}_{cal} \tilde{\mathbf{x}} \tilde{\mathbf{x}}^H \mathbf{K}_{cal} \mathbf{c}_\mu \quad (14)$$

can be minimized:

$$\mathbf{K}_{cal} = \min_{\mathbf{K}_{cal}} (\varepsilon^2(\mathbf{K}_{cal})) \quad (15)$$

Since the array error model (13) does not completely match all physical error sources and since the measurement noise \mathbf{n} cannot be avoided, only an estimate $\hat{\mathbf{K}}_{cal}$ can be obtained.

To achieve a useful computational form the next step is a matrix-vector exchange [1]. This allows a simple numerical solution of the optimization problem by an eigenvalue decomposition. After applying the matrix-vector-exchange to $\hat{\mathbf{K}}_{cal} \Rightarrow \hat{\mathbf{k}}_{cal}$ and the reverse one to $\mathbf{c}_\mu \Rightarrow \mathbf{O}_\mu$, (14) can be rewritten to:

$$\varepsilon^2 = \sum_{\mu=1}^{MN-1} \hat{\mathbf{k}}_{cal} \tilde{\mathbf{R}}_\mu \hat{\mathbf{k}}_{cal}^H \quad (16)$$

with covariance matrix $\tilde{\mathbf{R}}_\mu = \mathbf{O}_\mu^H \tilde{\mathbf{x}} \tilde{\mathbf{x}}^H \mathbf{O}_\mu$.

In order to enhance the rank of the covariance matrix and to further increase the stability of the estimate $\hat{\mathbf{k}}_{cal}$ that minimizes $\tilde{\mathbf{R}}$ an averaging over $v=1(1)D$ scenarios of different source directions should be applied:

$$\tilde{\mathbf{R}} = \sum_{v=1}^D \sum_{\mu=1}^{MN-1} \hat{\mathbf{k}}_{cal} \tilde{\mathbf{R}}_{v\mu} \hat{\mathbf{k}}_{cal}^H \quad (17)$$

The decomposition of (17) leads to $\hat{\mathbf{k}}_{cal}$ which is equivalent to that eigenvector having the smallest eigenvalue to fulfill the minimization. Finally the reverse matrix-vector-exchange to $\hat{\mathbf{k}}_{cal} \Rightarrow \hat{\mathbf{K}}_{cal}$ is required.

3.3 Calibration Procedure

The calibration measurement procedure is based on a set of D reference measurements in a well-defined anechoic environment. A minimum distance between the reference source antenna and the URA of approximately 100λ is chosen to get nearly plane wavefronts at the antenna array [5]. The reference antenna may be placed on an equiangular mesh of known elevation and azimuth angles α_v and β_v , within the array elevation and azimuth sector of interest. Zero degree for both, elevation and azimuth, stands for the broadside bearing of the URA. Actually, the reference antenna is kept fixed at $\alpha=\beta=0^\circ$ for simplification and the URA is rotated in its vertical and horizontal axes within the radiation center (cf. Fig. 7). For each reference measurement v the exact URA orientation described by η_v, ρ_v has to be known. Since the algorithm is based on a null steering approach the calibration result is sensitive against geometrical errors.

After collecting the measurement data the calibration algorithm is used to determine the calibration matrix. Thereby the dependencies between the phase characteristic θ resp. φ and the adjusted URA orientation discussed in 3.1 have to be taken into account. A regular measurement grid in η and ρ for the URA rotation leads to a distorted phase characteristic grid (see Fig. 9) based on (9) and (10).

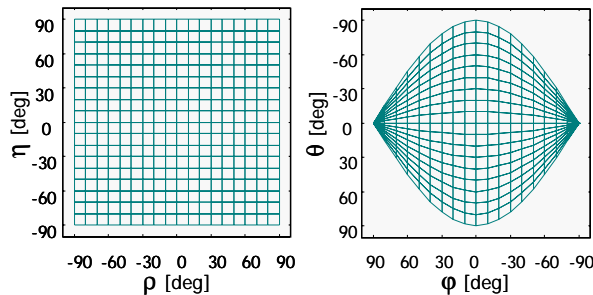


Fig. 9 Tilt angles and rotation angles at the URA vs. the resulting phase characteristics

After performing the calibration algorithm the resulting calibration matrix should be characterized by a structure mentioned in Fig. 8. Special matrix structures instead of the full matrix may be used since this requires only the definition of a proper matrix-vector-exchange. Nonrelevant coefficients may be set to zero and equivalent coefficients are set to be equal. Hence, it is reasonable

to omit coefficients which only describe a weak coupling. Additionally that modification may result in a significant reduction of the computational complexity because of the lower number of coefficients to be calculated.

In the following section the results of calibration measurements are presented. Additionally the performance of the calibrated URA is demonstrated using a critical coherent sources scenario.

4 Calibration Measurement Results

The measurement data are based on a measurement campaign carried out in an anechoic chamber with the wideband vector radio channel sounder RUSK [2]. The URA has been adjusted regarding its normal vector (Fig. 7) in a tilt angle range of -30° to $+30^\circ$ and in a rotation angle range of -60° to $+60^\circ$. The distance between the radiation center of the URA and the transmit antenna was approximately 7,50 m corresponding to 130λ .

The application of the 2-D calibration algorithm given in section 3.2 leads to the calibration matrix shown in Fig. 10. The structure of the matrix corresponds to that given in Fig. 8. The strongest element coupling (between neighboring elements) amounts to approximately -15 dB or below. This demonstrates the excellent performance of the array design presented in section 2 aiming at a minimum element coupling.

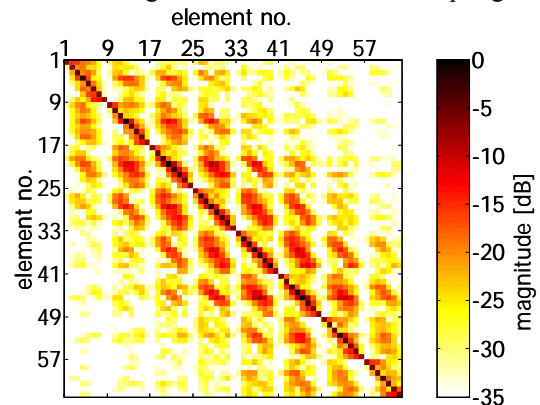


Fig. 10 Estimated calibration matrix (magnitude)

Applying the calibration matrix from Fig. 10 the calibrated URA beam pattern illustrated in the middle of Fig. 11 results. It can be seen clearly, that the beam pattern of the URA becomes more uniform for better fulfilling the beam pattern requirements of the ESPRIT algorithm. There is no need for a special shaped beam pattern but the uniform behavior of all elements is required. And indeed, the parameter estimation results compared to the source location relative to the URA bearing angle (depicted in Fig. 12) demonstrate a good behavior in the adjusted tilt and rotation range.

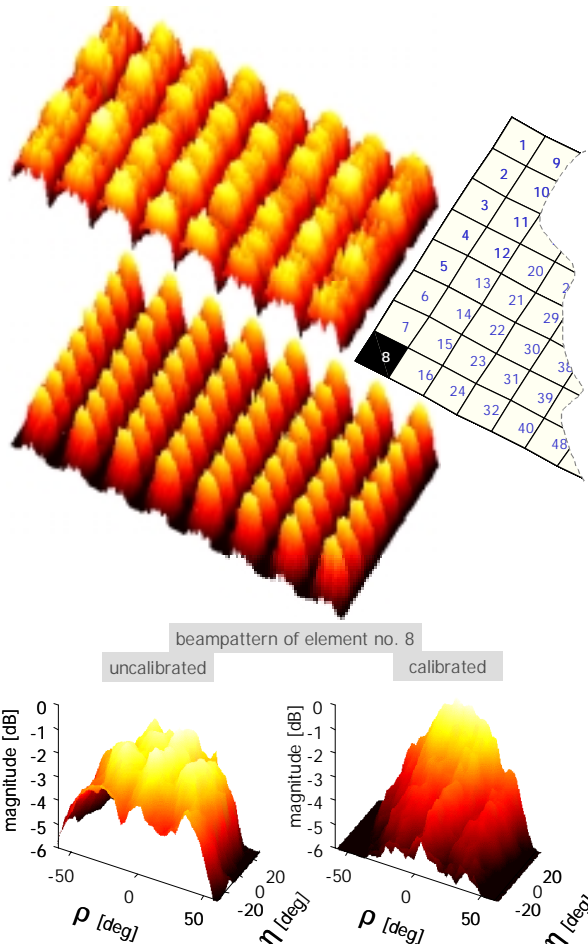


Fig. 11 Calibration result: uncalibrated element beampattern (top left) and below the calibrated one; scheme of the underlying URA (top right); exemplary zoomed beampattern of element no. 8 (bottom) – left uncalibrated and right calibrated

So far only a single source scenario has been considered validating the URA performance. However, in practice (e.g. in indoor environments) the spatial resolvability of coherent sources in time-delay might be more important. To investigate that, a measurement similar to that of the calibration has been performed, except that two sources were used. They have been placed at 2.5° resp. -2.5° in elevation and at 2.5° resp. -2.5° in azimuth. Using the calibration matrix (based on the calibration measurement) the measurement data can be calibrated. After that, they have been processed by the 2-D ESPRIT algorithm in order to validate their known positions (cf. Fig. 13). The estimation results demonstrate the high quality of the calibrated antenna array within the adjusted tilt and rotation range.

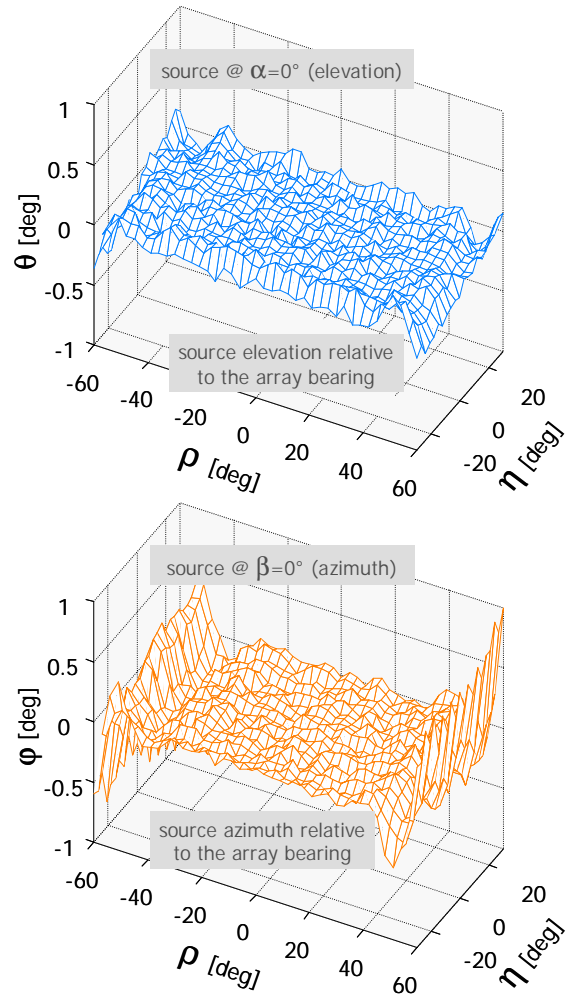


Fig. 12 Parameter estimation results based on 2-D Unitary ESPRIT (top: DoA in elevation resp. θ ; bottom: DoA in azimuth resp. φ) – the DoAs have been compensated by the known URA orientation characterized by η and ρ

5 Conclusions

In this paper the antenna design and the 2-D calibration approach for URAs have been analyzed for ESPRIT-type DoA estimation applications. They have been verified by calibration measurements in an anechoic environment. It turned out, that this approach improves considerably the array performance which can be seen from an increased accuracy of DoAs in azimuth and elevation estimated by the unitary 2-D ESPRIT algorithm. The calibration approach consists of a set of single source reference measurements and of a least squares estimation of a calibration matrix. The result is a calibration matrix that equalizes all array outputs.

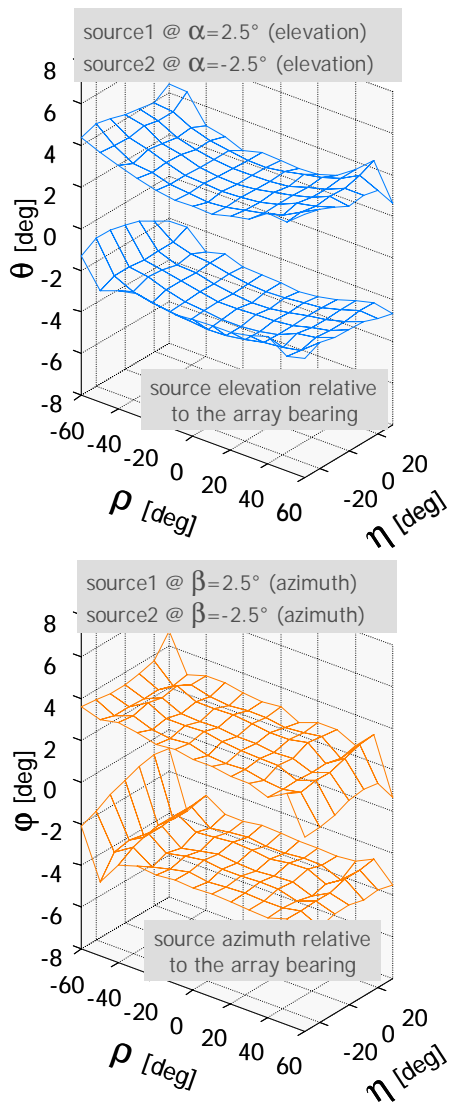


Fig. 13 Parameter estimation results based on 2-D Unitary ESPRIT (top: DoAs in elevation of the two coherent sources; bottom: DoAs in azimuth of the two coherent sources) – the DoAs have been compensated by the known URA orientation characterized by η and ρ

Acknowledgements

The authors wish to thank Prof. Rembold and his colleagues from the RWTH Aachen for supporting the measurements in the anechoic chamber.

6 Literature

- [1] K. Pensele and J.A. Nossek: „Uplink and Downlink Calibration of Smart Antennas,” Proc. Int. Conf. on Telecomm. (ICT98), Porto Carras, Greece, June 1998.
- [2] R.S. Thomä, D. Hampicke, A. Richter, G. Sommerkorn, A. Schneider, U. Trautwein, W. Wirmitzer: „Identification of Time-Variant Directional Mobile Radio Channels,” IEEE Trans. on Instrumentation and Measurement, Vol.49, pp. 357-364, April 2000.
- [3] G. Sommerkorn, D. Hampicke, R. Klukas, A. Richter, A. Schneider, R. Thomä: „Reduction of DoA Estimation Errors Caused by Antenna Array Imperfections,” Proc. 29th European Microwave Conference, Munich, Vol. 2, pp. 287-290, Oct. 4-8, 1999.
- [4] M. Haardt: „Efficient One-, Two-, and Multidimensional High-Resolution Array Signal Processing,” Ph.D. Thesis, Shaker Verlag, ISBN 3-8265-2220-6, Aachen, Germany, 1996.
- [5] P. Lehne, F. Aanvik, J.-C. Bie, P. Pajusco, M. Grigat, I. Gaspard, U. Martin: „Calibration of Mobile Radio Channel Sounders,” COST 259, TD-98, Duisburg, Germany, Sept. 1998.